

**$L1_0$ -ordered  $(\text{Fe}_{100-x}\text{Cr}_x)\text{Pt}$  thin films: Phase formation, morphology, and spin structure**

Nataliia Y. Schmidt <sup>1</sup>, Ritwik Mondal <sup>2</sup>, Andreas Donges,<sup>2</sup> Julian Hintermayr <sup>1</sup>, Chen Luo <sup>3,4</sup>, Hanjo Ryll,<sup>4</sup> Florin Radu,<sup>4</sup> László Szunyogh <sup>5,6</sup>, Ulrich Nowak <sup>2</sup> and Manfred Albrecht <sup>1</sup>

<sup>1</sup>*Institute of Physics, University of Augsburg, Universitätsstrasse 1, D-86159, Augsburg, Germany*

<sup>2</sup>*Department of Physics, University of Konstanz, D-78457 Konstanz, Germany*

<sup>3</sup>*Experimental Physics of Functional Spin Systems, Technische Universität München, James-Frank-Str. 1, D-85748 Garching b. München, Germany*

<sup>4</sup>*Helmholtz-Zentrum Berlin, D-14109 Berlin, Germany*

<sup>5</sup>*Department of Theoretical Physics, Budapest University of Technology and Economics, Budafoki út 8, H-1111 Budapest, Hungary*

<sup>6</sup>*MTA-BME Condensed Matter Research Group, Budapest University of Technology and Economics, Budafoki út 8, H-1111 Budapest, Hungary*



(Received 6 August 2020; accepted 4 December 2020; published 28 December 2020)

Chemically ordered  $L1_0$   $(\text{Fe}_{100-x}\text{Cr}_x)\text{Pt}$  thin films were epitaxially grown on  $\text{MgO}(001)$  substrates by magnetron sputter-deposition at  $770^\circ\text{C}$ . In this sample series, Fe was continuously substituted by Cr over the full composition range. The lattice parameter in the  $[001]$  growth direction steadily increases from  $L1_0$ -FePt toward  $L1_0$ -CrPt, confirming the incorporation of Cr in the lattice occupying Fe sites. With the observed high degree of chemical ordering and  $(001)$  orientation, strong perpendicular magnetic anisotropy is associated, which persists up to a Cr content of  $x = 20$  at. %. Similarly, the coercive field in the easy-axis direction is strongly reduced, which is, however, further attributed to a strong alteration of the film morphology with Cr substitution. The latter changes from a well-separated island microstructure to a more continuous film morphology. In the dilute alloy with low Cr content, isolated Cr magnetic moments couple antiferromagnetically to the ferromagnetic Fe matrix. In this case, all Cr moments are aligned parallel, thus forming a ferrimagnetic FeCrPt system. With increasing Cr concentration, nearest-neighbor Cr-Cr pairs start to appear, thereby increasing magnetic frustration and disorder, which lead to canting of neighboring magnetic moments, as revealed by atomistic spin-model simulations with model parameters based on first principles. At higher Cr concentrations, a frustrated ferrimagnetic order is established. With Cr substitution of up to 20 at. %, no pronounced change in Curie temperature, which is in the range of 700 K, was noticed. But with further addition the Curie temperature drops down substantially even down to room temperature at 47 at. % Cr. Furthermore, x-ray magnetic circular dichroism studies on dilute alloys containing up to 20 at. % of Cr revealed similar spin moments for Fe and Cr in the range between  $2.1$ – $2.5 \mu_B$  but rather large orbital moments of up to  $0.50 \pm 0.10 \mu_B$  for Cr. These results were also compared to *ab initio* calculations.

DOI: [10.1103/PhysRevB.102.214436](https://doi.org/10.1103/PhysRevB.102.214436)

## I. INTRODUCTION

FePt alloy thin films with chemically ordered  $L1_0$  structure have been investigated intensively for high-density magnetic recording media [1–5] and magnetic random access memory applications [6,7] due to their large magnetocrystalline anisotropy energies, providing high thermal stability of magnetization against thermal fluctuations. The ordered structure consists of alternate stacking of Fe and Pt atoms along the  $c$  axis of the face-centered tetragonal structure. As the easy magnetization axis of the  $L1_0$  crystal is parallel to the  $c$  axis, a  $(001)$  orientation is mandatory for practical device applications requiring perpendicular magnetic anisotropy. Despite the large lattice misfit of about 9%,  $\text{MgO}(001)$  substrates [8,9] or seed layers [10–12] are commonly employed for epitaxial growth of  $L1_0$  FePt(001). Typically, for film deposition, a substrate temperature higher than  $500^\circ\text{C}$  is required to promote  $L1_0$  order, while lower

temperatures result in the chemically disordered fcc (A1) structure.

As key magnetic properties such as uniaxial magnetic anisotropy ( $K_u$ ), saturation magnetization ( $M_S$ ), and Curie temperature ( $T_C$ ) are not fully independent, adjustment and optimization of these parameters are of supreme importance for applications. One promising route is the substitution with third elements into the  $L1_0$  FePt lattice. For instance, partial substitution of Fe with Cu occupying Fe sites induce lowering of the ordering temperature and reduction of  $T_C$  [13–19], which is attractive for heat-assisted magnetic recording [2,3]. However,  $K_u$  and  $M_S$  are lowered as well, thus a delicate tuning of the Cu concentration is necessary for applications. A recent theoretical work [20] studied the effect of substituting Fe by various  $3d$  transition metal (TM) elements (i.e., Cr, Mn, Co, Ni, Cu), whose introduction changes the effective number of valence electrons and thus allows tuning of the magnetic anisotropy energy (MAE). However, these studies need to be

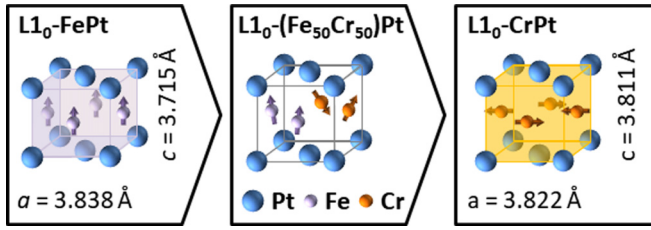


FIG. 1. Schematic picture of the ferromagnetic  $L1_0$ -FePt structure, intermediate ferrimagnetic  $L1_0$  unit cell with substitution of Fe by Cr, where frustration leads to spin canting, and the antiferromagnetic  $L1_0$  CrPt structure.

supported by experiments that also consider the chemical and structural changes induced by third element doping.

Another important characteristic is the difference in the magnetic exchange interaction. While Ni couples ferromagnetically to the Fe matrix [21–24], antiferromagnetic coupling is expected for Mn [25–27] and Cr [28,29]. For the latter case, complex spin structures are expected. In this regard, frustration and spin canting should arise from the competition of ferromagnetic Fe-Fe, antiferromagnetic Cr-Cr (Mn-Mn), as well as antiferromagnetic Cr(Mn)-Fe nearest-neighbor exchange interactions, depending on the concentration [28,30]. This magnetic frustration is expected to reduce the saturation magnetization and lower the effective Curie temperature [30]. Schematics of various spin structures are illustrated in Fig. 1, showing the expected transition from ferromagnetic  $L1_0$  FePt to antiferrimagnetic  $L1_0$  CrPt magnetic order [31] via a magnetically disordered ferrimagnetic state upon Cr addition.

Experimentally, the magnetic and structural properties of epitaxial  $(\text{Fe}_{100-x}\text{Mn}_x)\text{Pt}$  ( $0 \leq x \leq 68$ ) thin films were investigated in detail by Meyer and Thiele [25]. Maximum magnetic anisotropy and magnetization were reported for the pure FePt alloy, and substitution with Mn resulted in a steady reduction of magnetocrystalline anisotropy, Curie temperature, and saturation magnetization, the latter being a result of antiparallel alignment of Fe and Mn moments. Further, it was reported by Kuo *et al.* for nonstoichiometric  $(\text{FePt})_{100-x}\text{Cr}_x$  thin films that the addition of Cr also leads to a reduction of magnetization and coercivity, but also inhibits grain growth during annealing [32]. These films were sputter deposited at room temperature on natural-oxidized Si(111) substrates and postannealed up to 750 °C for 15 min showing strong (111) texture and the presence of further phases, e.g., Al FePt and FeCr.

Here, a systematic study on the evolution of magnetic and structural properties of epitaxial  $(\text{Fe}_{100-x}\text{Cr}_x)\text{Pt}$  thin films covering the full composition range is presented. Different exchange interactions between Cr-Cr, Cr-Fe, and Fe-Fe pairs stimulates magnetic frustration and spin canting, which was investigated in more detail by *ab initio* and atomistic spin-model calculations.

## II. EXPERIMENTAL AND THEORETICAL METHODS

### A. Preparation

A series of  $(\text{Fe}_{100-x}\text{Cr}_x)\text{Pt}$  thin alloy films was deposited by magnetron cosputtering from individual Fe, Pt, and Cr

targets on MgO(001) substrates at 770 °C using an Ar working pressure of 5  $\mu\text{bar}$ . The Cr content  $x$  was varied between 0–100 at. % by altering the deposition rates while keeping the (Fe+Cr) to Pt ratio roughly equal. An overview of the sample names and corresponding composition and film thickness, as evaluated by Rutherford backscattering spectrometry, is given in Table I. All samples in the series are protected from surface oxidation by a 3-nm-thick Al capping layer. The surface morphology of the samples was investigated by scanning electron microscopy (SEM).

The evolution of the  $L1_0$  phase formation was studied by x-ray diffraction (XRD) using  $\text{Cu-K}\alpha$  radiation. The chemical order parameter  $S$  was calculated as  $S = \sqrt{(I_{(001)}^{\text{exp}} I_{(002)}^{\text{theo}}) / (I_{(001)}^{\text{theo}} I_{(002)}^{\text{exp}})}$ , using the ratio of theoretical ( $I^{\text{theo}}$ ) and experimental ( $I^{\text{exp}}$ ) integrated intensities [33].  $I_{(001)}^{\text{exp}}$  and  $I_{(002)}^{\text{exp}}$  are the integrated intensities of the respective reflections, corrected for absorption, Lorentz, Debye-Waller, and angular-dependent atomic scattering factors. The structure factor was calculated assuming a pseudobinary TM:Pt alloy, where Fe and Cr atoms are randomly distributed among TM sites. An experimental Debye-Waller factor of 0.0136 nm, reported for  $L1_0$  FePt [34], was used for all samples. The linear attenuation factor, required to compute the absorption factor, was estimated from weighted elemental mass absorption factors in combination with the assessed unit cell volume  $a^2c$ . For this, a value of  $a$  in the range of  $0.97 - 0.99c$  was assumed for varying Cr content. The order parameter is normalized to the calculated maximum value,  $S_{\text{Max}} = 1 - 2\Delta$ , where  $\Delta$  is the deviation from the elemental 50:50 ratio of TM:Pt content. Please note that in addition to conventional error calculations, an additional error on the experimental ratio of intensities of up to  $\pm 0.1$  was added due to overlap of the  $L1_0$ -(002) peak with the main substrate reflection and possibly present (020) reflections, especially on the Cr-rich side.

### B. Magnetic measurements

Static magnetic properties were characterized using a superconducting quantum interference device-vibrating sample magnetometer (SQUID-VSM) in the temperature range of 25–800 K. For selected samples, x-ray magnetic circular dichroism (XMCD) absorption experiments were performed at the high-field end station VEKMAG [35] installed at the PM2 beamline of the Helmholtz-Zentrum Berlin (HZB). XAS spectra were collected at the Fe and Cr  $L_{2,3}$  edges using the total electron yield (TEY) detection mode. The XMCD signal was calculated as the difference between XAS spectra measured with two opposite directions of the external magnetic field of up to  $\pm 80$  kOe. Besides evaluating spin and orbital moments of Cr and Fe, element-specific magnetic hysteresis loops were measured at room temperature for both Fe and Cr at the energy of maximum XMCD signal.

### C. *Ab initio* calculations

The magnetic moments, exchange interactions, and magnetic anisotropy energies were calculated by density functional theory (DFT) within the local spin density approximation (LSDA) [36]. First, self-consistent calculations were performed using the fully relativistic screened

TABLE I. Overview of the structural and magnetic properties of the (Fe<sub>100-x</sub>Cr<sub>x</sub>)Pt sample series at room temperature. Film composition (uncertainty  $\pm 2$  at. %) and thickness (uncertainty 10%) was determined by Rutherford backscattering spectrometry.

Sample name	Fe (at. %)	Pt (at. %)	Cr (at. %)	$t$ (nm)	$S$	$c/a$	$M_S$ (emu/cm <sup>3</sup> )	$K_u$ (Merg/cm <sup>3</sup> )	$H_C$ (kOe)	$T_C$ (K)
Fe <sub>52</sub> Pt <sub>48</sub>	52	48	–	10	0.93	0.964	1092	22.8	42.9	707
(Fe <sub>89</sub> Cr <sub>11</sub> )Pt	47	47	6	9	0.91	0.965	1037	19.9	22.8	719
(Fe <sub>85</sub> Cr <sub>15</sub> )Pt	45	47	8	9	0.81	0.965	1016	20.3	16.7	692
(Fe <sub>80</sub> Cr <sub>20</sub> )Pt	43	46	11	10	0.91	0.971	890	12.9	10.8	653
(Fe <sub>65</sub> Cr <sub>35</sub> )Pt	33	49	18	10	0.54	0.976	680	1.6	0.2	504
(Fe <sub>53</sub> Cr <sub>47</sub> )Pt	27	49	24	10	0.51	0.980	226	–	–	300
(Fe <sub>42</sub> Cr <sub>58</sub> )Pt	22	48	30	10	0.34	0.982	<70	–	–	–
(Fe <sub>31</sub> Cr <sub>69</sub> )Pt	16	49	35	10	0.34	0.988	<50	–	–	–
(Fe <sub>20</sub> Cr <sub>80</sub> )Pt	10	49	41	10	0.39	0.991	<50	–	–	–
Cr <sub>52</sub> Pt <sub>48</sub>	–	48	52	9	0.41	0.987	<50	–	–	–

Korringa-Kohn-Rostoker method [37–39] employing the atomic sphere approximation by expanding the partial waves up to  $l_{\max} = 2$  (*spd* basis) inside the atomic spheres. The MAE and the exchange interactions were then determined by means of the magnetic force theorem [39,40].

The (Fe<sub>100-x</sub>Cr<sub>x</sub>)Pt films were modeled in the bulk geometry in the *ab initio* calculations. We considered the systems with low Cr content,  $0 \leq x \leq 40$  at. %, and for each concentration the lattice parameters  $a = 3.863$  Å and  $c = 3.784$  Å, resulting in a  $c/a$  ratio of 0.979 of FePt were used, as in previous theoretical works [41,42]. Random distribution of the Fe and Cr atoms was supposed in the nominal Fe layers of FePt, which was treated in terms of the coherent potential approximation [43]. Chemical disorder with respect to intermixing of the Fe<sub>100-x</sub>Cr<sub>x</sub> and the Pt layers was not considered in the calculations.

#### D. Spin dynamics simulation

Furthermore, to extract the magnetic properties of the Cr doped FePt system in the ground state as well as at elevated temperatures, the stochastic Landau-Lifshitz-Gilbert (LLG) equation of motion via atomistic spin simulations was solved,

$$\frac{\partial \mathbf{s}_i}{\partial t} = -\frac{\gamma}{(1 + \alpha^2)\mu_i^s} \mathbf{s}_i \times [\mathbf{H}_i^{\text{eff}} + \alpha \mathbf{s}_i \times \mathbf{H}_i^{\text{eff}}], \quad (1)$$

using a Heun's algorithm [44,45]. The LLG equation contains a gyromagnetic ratio  $\gamma = 1.76 \times 10^{11}$  T<sup>-1</sup> sec<sup>-1</sup>, magnetic moment  $\mu_i^s$ , and a scalar damping parameter  $\alpha$  that accounts for the energy dissipation to a heat bath. The effective field  $\mathbf{H}_i^{\text{eff}}$  can be calculated by using the total energy ( $\mathcal{H}$ ) of the system as

$$\mathbf{H}_i^{\text{eff}} = \zeta_i(t) - \frac{\partial \mathcal{H}}{\partial \mathbf{s}_i}. \quad (2)$$

To account for the influence of the temperature  $T$ , a stochastic white noise term  $\zeta_i(t)$  was introduced, which obeys the following properties:

$$\langle \zeta_i(t) \rangle = 0, \quad (3)$$

$$\langle \zeta_i^\eta(t) \zeta_j^\theta(t') \rangle = \frac{2k_B T \alpha \mu_i^s}{\gamma} \delta_{ij} \delta_{\eta\theta} \delta(t - t'), \quad (4)$$

with  $k_B$  as Boltzmann constant and the indices  $\{i, j\}$  and  $\{\eta, \theta\}$  represent the atomic lattice sites and components of the stochastic noise field. To account for the total energy, the Hamiltonian

$$\mathcal{H} = -\sum_{i \neq j} J_{ij} \mathbf{s}_i \cdot \mathbf{s}_j - \sum_i K_u s_{iz}^2 - \sum_i \mu_i^s \mathbf{B}_i \cdot \mathbf{s}_i \quad (5)$$

was considered, where the three energy terms describe the Heisenberg exchange parameters ( $J_{ij}$ ), the uniaxial magnetic anisotropy constant ( $K_u$ ), and the Zeeman energy, respectively.

### III. STRUCTURAL PROPERTIES AND MICROSTRUCTURE

XRD ( $\theta - 2\theta$ ) scans of the (Fe<sub>100-x</sub>Cr<sub>x</sub>)Pt sample series are displayed in Fig. 2. The reference FePt sample shows pronounced (001) superstructure and (002) reflections, characteristic for the chemically ordered L1<sub>0</sub>-FePt structure. With addition of Cr, no apparent changes of the diffractograms are observed, maintaining the L1<sub>0</sub> structure over the whole composition range. The  $a$ - and  $c$ -lattice parameters were extracted from the (111) and L1<sub>0</sub>-(001) superstructure reflection positions, respectively. While the  $a$ -lattice parameter is close to bulk L1<sub>0</sub>-FePt and remains almost constant, the  $c$ -lattice parameter starting from pure bulk L1<sub>0</sub>-FePt ( $c = 0.371$  nm) is continuously increasing with Cr addition, indicating the incorporation of Cr into the L1<sub>0</sub>-FePt lattice [Fig. 3(a)]. For higher Cr content, the lattice parameter approaches the value of L1<sub>0</sub>-CrPt (bulk  $c = 0.381$  nm) [46]. Initially, a linear increase with Cr content up to 20 at. %, following Vegard's law for a solid solution, is observed. However, with further Cr addition some deviation occurs. The higher Pt concentration in these alloys is most likely the reason for that, but it should be noticed that this law is seldom perfectly obeyed, as discussed in Refs. [47,48]. The evaluation of the L1<sub>0</sub> order parameter for the FePt reference layer revealed a high degree of ordering with a value of 0.93, which is close to the theoretical maximum  $S_{\max}$  of 1 [Fig. 3(b)]. This high degree of order remains for film samples up to 20 at. % Cr. With further increase of Cr content, the order parameter gets reduced down to about 0.3–0.4. In this regard, in an earlier study on L1<sub>0</sub> CrPt phase formation, it was reported that L1<sub>0</sub> ordering is quite limited when grown at elevated temperatures up to 770 °C compared to postannealed

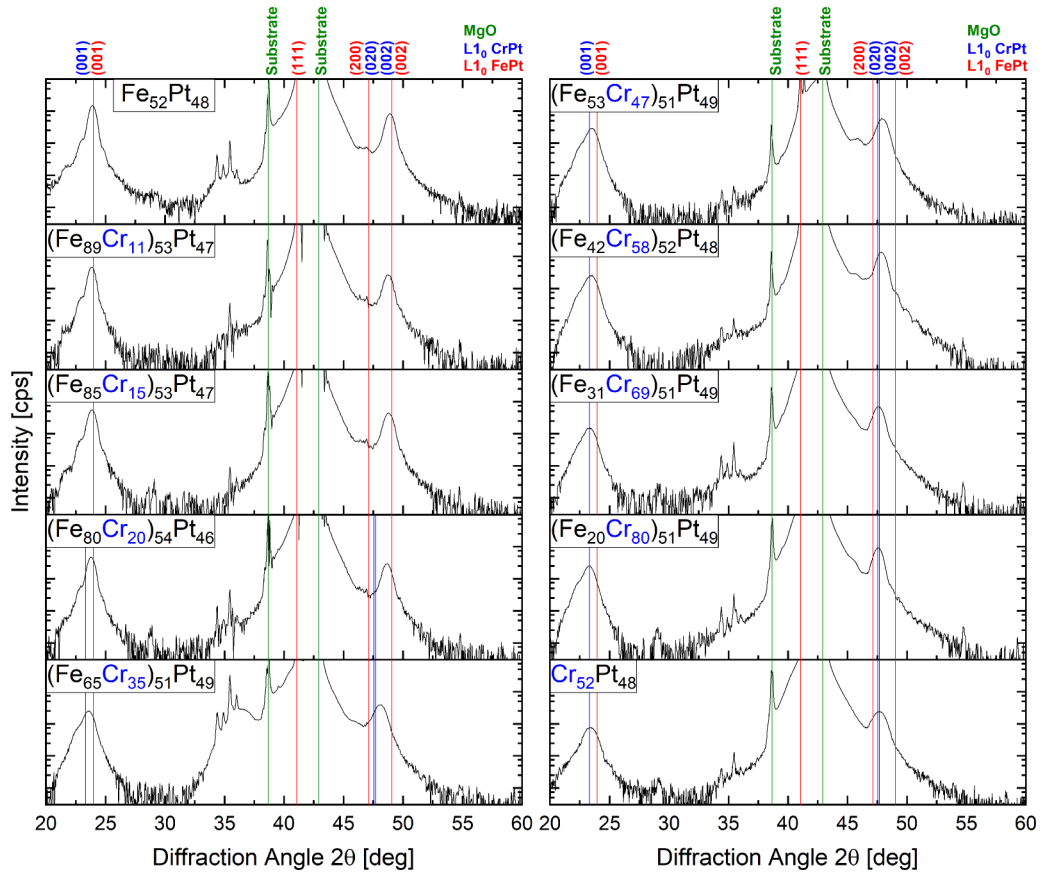


FIG. 2. XRD ( $\theta - 2\theta$ )-scans of the  $(\text{Fe}_{100-x}\text{Cr}_x)\text{Pt}$  sample series. The additional weak peaks between  $2\theta = 28.8^\circ - 29.2^\circ$  are substrate related.

samples [49]. Thus, in contrast to FePt, for CrPt even higher deposition temperatures are required for sufficient  $L1_0$  phase formation.

To investigate the microstructure in detail, SEM imaging was performed, as displayed in Fig. 4. For reference,  $L1_0$ -FePt film pronounced agglomeration with well-separated islands is found. Most of the individual islands cover an averaged area of about  $2 \times 10^{-2} \mu\text{m}^2$  but with a broad distribution in sizes. The lattice misfit with respect to the MgO crystal is about  $-9\%$  (tensile stress) and both materials have very similar thermal expansion coefficients [50]. Together with a larger surface energy of FePt [51] compared to MgO [52], the formation of an isolated island morphology when grown at high temperatures is favored. Adding Cr up to 20 at. % shows almost no changes in average island size [Figs. 4(b)–4(d)]. However, with substitution of Fe by 35 at. % Cr, the morphology changes drastically: Instead of island growth, the film appears more continuous with hole structures—large elongated ones extended over an area of up to  $4.5 \times 10^{-2} \mu\text{m}^2$  and small ones with a diameter of about 10 nm [Fig. 4(e)]. With further increase in Cr content, the elongated holes shrink in size while the density of the small holes increases steadily [Figs. 4(f)–4(h)] until they mostly vanish for pure  $L1_0$ -CrPt. It is well known for thin films that surface and interface tension effects play a major role in determining the overall stability of a film to agglomeration [53]. Further, it is generally observed that tensile stresses within a film can enhance hole formation/agglomeration, while compressive stresses often

lead to hillock formation. Both provide stress relaxation in the film. It is speculated that reduced tensile stress with addition of Cr leads to the observed change in morphology. However, due to the lack of literature data, it is hard to relate the microstructure to all these varying contributions.

#### IV. STATIC MAGNETIC PROPERTIES

Room-temperature  $M$ - $H$  hysteresis loops of the  $(\text{Fe}_{100-x}\text{Cr}_x)\text{Pt}$  sample series obtained in in-plane (ip) and out-of-plane (oop) geometry are shown in Fig. 5. Samples with up to 20 at. % Cr reveal strong uniaxial magnetic anisotropy with an easy axis of magnetization in the out-of-plane direction. The effective magnetic anisotropy  $K_{\text{eff}}$  was extracted from the differences of the areas enclosed by the averaged hard axis (ip) and easy axis (oop) loops and the magnetization axis of the  $M$ - $H$  loops. The uniaxial magnetic anisotropy  $K_u$  was calculated as the sum of  $K_{\text{eff}}$  and the magnetic shape anisotropy ( $K_{\text{sh}} = 2\pi \cdot M_s^2$ ). Values of  $K_{\text{eff}}$  and  $K_u$  obtained at room temperature are summarized in Figs. 6(a) and 6(b), respectively. Films with up to 20 at. % Cr show strong perpendicular magnetic anisotropy which gets gradually reduced from 23 down to 13 Merg/cm<sup>3</sup> with increasing Cr content. However, at 35 at. % of Cr, the uniaxial magnetic anisotropy drops almost to zero. A similar behavior is observed for the coercivity, which continuously decreases from 43 down to 11 kOe for up to 20 at. % Cr and almost vanishes at 35 at. % Cr [Fig. 6(d)].

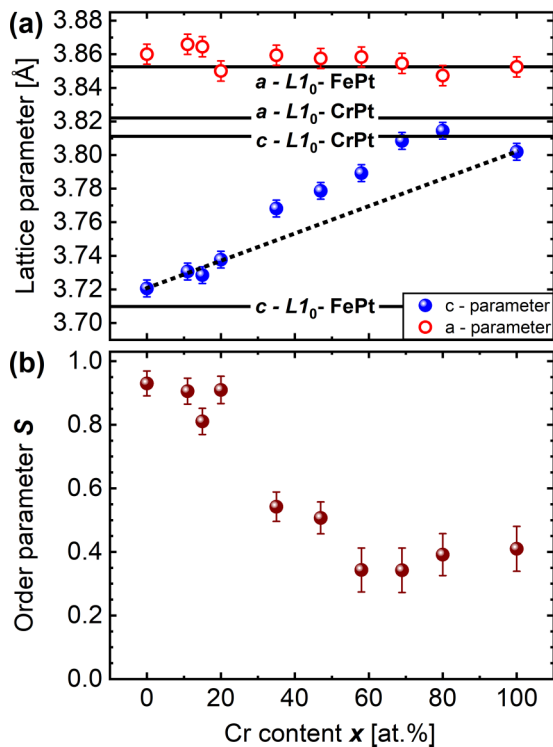


FIG. 3. (a)  $a$ - and  $c$ -lattice parameters and (b) order parameter  $S$  of the  $(\text{Fe}_{100-x}\text{Cr}_x)\text{Pt}$  sample series in dependence of the Cr content  $x$ . Solid lines mark the bulk values of the  $c$ -lattice parameter for  $L1_0$ -FePt and  $L1_0$ -CrPt while the dotted line follows Vegard's law.

Of particular interest is the evolution of the saturation magnetization  $M_S$ . At low Cr concentration, a ferrimagnetic ground state is expected, as the Fe moments couple antiferromagnetically to the Cr moments. In this case, as the Cr is heavily diluted in the FePt matrix, an overall parallel alignment of the Cr moments is supposed. At higher concentrations, nearest-neighbor Cr-Cr pairs start to appear, thereby increasing magnetic frustration and disorder. Frustration arises from the competition of ferromagnetic Fe-Fe and antiferromagnetic Cr-Cr(Fe) nearest-neighbor (NN) exchange interactions, resulting in canting of neighboring magnetic moments, as will be discussed later in more detail by atomistic spin-model calculations. Nevertheless, in both cases a strong reduction in magnetization can be expected. Indeed, the saturation magnetization gets strongly reduced by almost 40% down to  $700 \text{ emu/cm}^3$  with doping by 35 at. % of Cr [Fig. 6(c)]. At an almost equiatomic Fe to Cr ratio, the  $M_S$  value becomes negligibly small due to the formation of antiferromagnetic order [31].

Additional magnetization versus temperature measurements were performed at temperatures up to 800 K to study the influence of Fe substitution by Cr on the Curie temperature [Fig. 7(a)]. For Cr concentrations below 20 at. %, no significant impact on  $T_C$  was observed revealing a value of about 700 K. However, further substitution of Fe with 35 and 47 at. % Cr lowers the magnetic ordering temperature substantially down to 500 and 300 K, respectively, as summarized in Fig. 7(b).

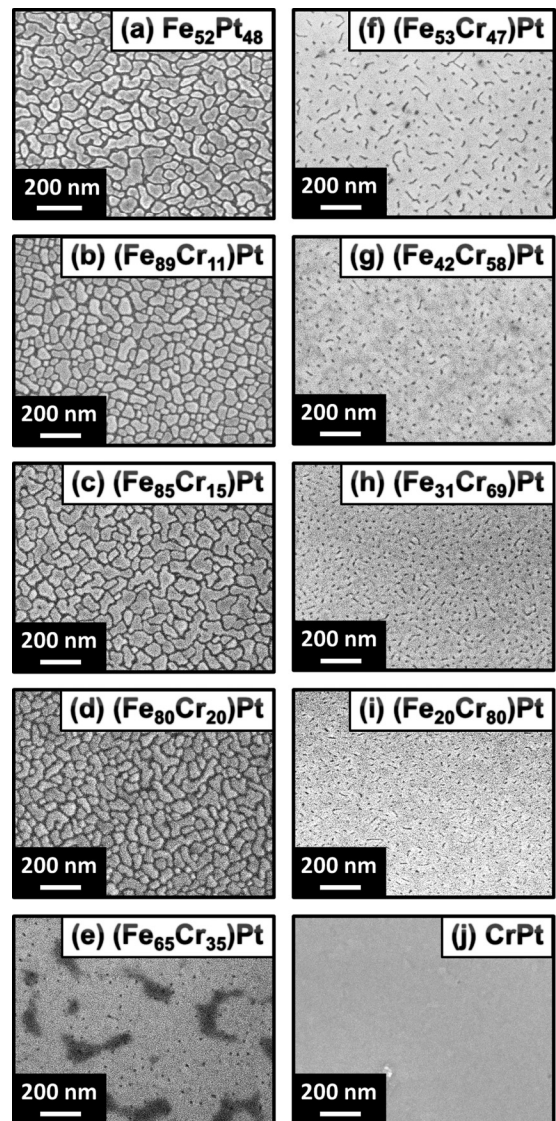


FIG. 4. (a)–(j) SEM images of the  $(\text{Fe}_{100-x}\text{Cr}_x)\text{Pt}$  sample series.

## V. X-RAY MAGNETIC CIRCULAR DICHROISM STUDY

To investigate the relative orientation of the magnetic moments between Fe and Cr and to evaluate their spin and orbital moments, XMCD measurements were performed at room temperature. The XMCD spectra at the Fe and Cr  $L_{2,3}$  edges are shown in Figs. 8(a) and 8(b), respectively. The resulting dichroism signals have opposite signs, indicating an antiparallel alignment of the Fe and Cr magnetic moments. Element-specific hysteresis loops, recorded in out-of-plane geometry for samples with perpendicular magnetic anisotropy (up to 20 at. % Cr), show exactly the same shape of magnetic reversal behavior but mirrored relatively to each other, which is due to strong antiferromagnetic exchange coupling [Figs. 8(c)–8(h)]. Furthermore, using sum rule considerations, the spin ( $\mu_s$ ) and orbital moments ( $\mu_l$ ) of Fe and Cr were calculated. The results are summarized in Table II. It was found that the Fe spin magnetic moment per atom is in the range of  $2.1$ – $2.5 \mu_B$  with a small orbital contribution of about  $0.1 \mu_B$ . For the Cr magnetic moments, values in a similar range

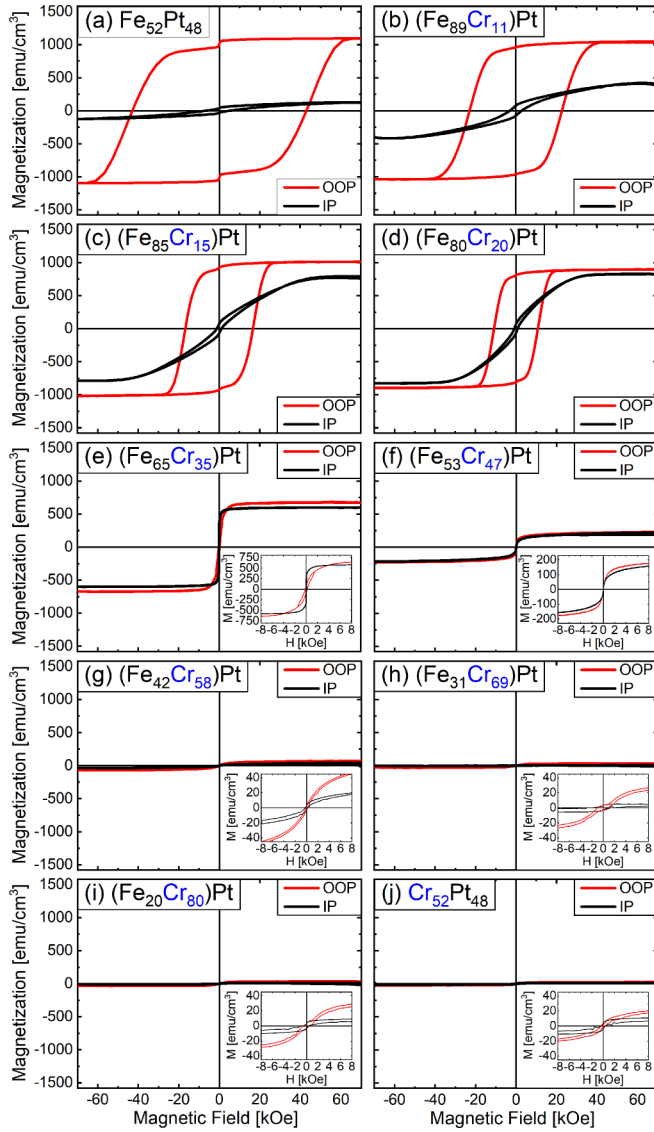


FIG. 5. (a)–(j)  $M$ - $H$  hysteresis loops measured in out-of-plane and in-plane geometry at 300 K for the  $(\text{Fe}_{100-x}\text{Cr}_x)\text{Pt}$  sample series. Insets show the enlarged central part of the corresponding loops.

TABLE II. Experimental spin ( $\mu_s$ ), orbital ( $\mu_l$ ), and total magnetic moment ( $\mu_{\text{total}} = \mu_s + \mu_l$ ) of Fe and Cr (per atom) of the  $(\text{Fe}_{100-x}\text{Cr}_x)\text{Pt}$  sample series.

Sample	Absorption edge	$\mu_s$ [ $\mu_B$ ]	$\mu_l$ [ $\mu_B$ ]	$\mu_{\text{total}}$ [ $\mu_B$ ]
$\text{Fe}_{52}\text{Pt}_{48}$	Fe	$2.29 \pm 0.23$	$0.14 \pm 0.01$	$2.43 \pm 0.24$
$(\text{Fe}_{89}\text{Cr}_{11})\text{Pt}$	Fe	$2.54 \pm 0.25$	$0.05 \pm 0.01$	$2.59 \pm 0.26$
	Cr	$2.43 \pm 0.35$	$0.30 \pm 0.05$	$2.73 \pm 0.40$
$(\text{Fe}_{85}\text{Cr}_{15})\text{Pt}$	Fe	$2.42 \pm 0.24$	$0.05 \pm 0.01$	$2.47 \pm 0.25$
	Cr	$2.50 \pm 0.38$	$0.34 \pm 0.05$	$2.84 \pm 0.43$
$(\text{Fe}_{80}\text{Cr}_{20})\text{Pt}$	Fe	$2.11 \pm 0.21$	$0.12 \pm 0.01$	$2.23 \pm 0.22$
	Cr	$2.36 \pm 0.47$	$0.50 \pm 0.10$	$2.86 \pm 0.57$

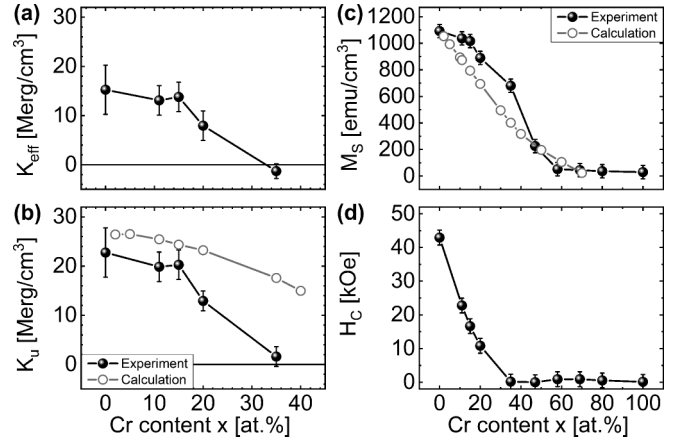


FIG. 6. Dependence of (a) effective and (b) uniaxial magnetic anisotropy, (c) saturation magnetization, and (d) coercive field on the Cr content. All values are obtained at 300 K. Results from *ab initio* calculations are included in (b) and (c).

between  $2.3$ – $2.5 \mu_B$  were obtained. The magnetic moments of Cr are comparable to values reported for bulk  $L1_0$ -CrPt alloys of  $2.24 \pm 0.15 \mu_B$  [31] but substantially larger than for epitaxial  $\text{Fe}_{1-x}\text{Cr}_x$  films of up to  $1.0 \pm 0.1 \mu_B$  [28]. Interestingly, a rather high orbital moment of up to  $0.5 \mu_B$  is observed for Cr.

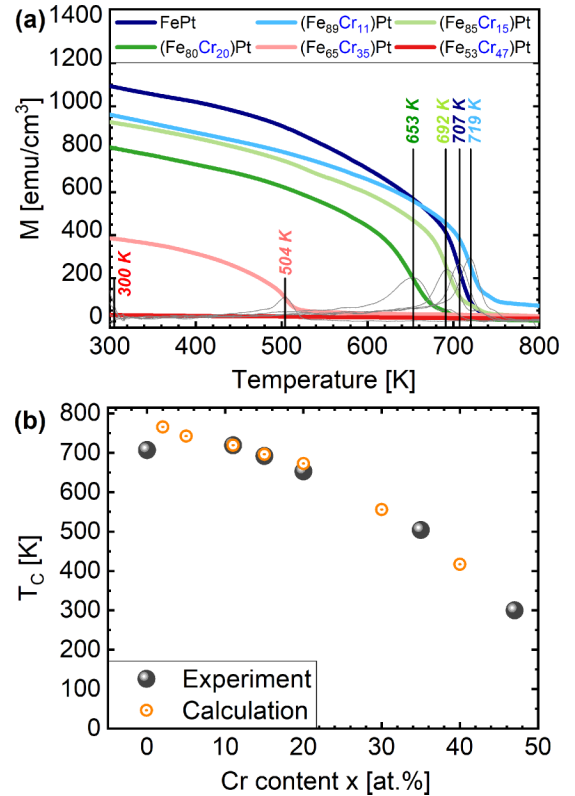


FIG. 7. (a) Magnetization versus temperature curves measured along the easy axis direction of the respective  $(\text{Fe}_{100-x}\text{Cr}_x)\text{Pt}$  sample. A guiding field of 100 Oe was applied during measurement. (b) Dependence of the Curie temperature on the Cr content including results from atomistic spin model calculations.

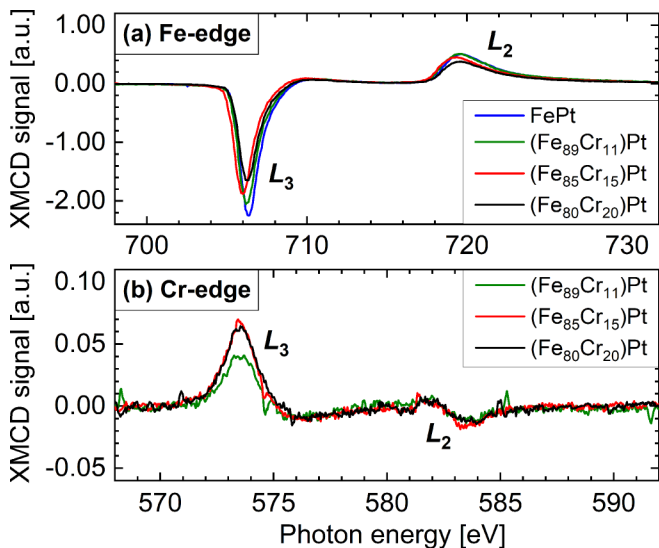


FIG. 8. XMCD spectra of (a) Fe and (b) Cr for the (Fe<sub>100-x</sub>Cr<sub>x</sub>)Pt sample series. (c)–(h) XMCD element-specific hysteresis loops for selected samples obtained at the Fe- (c), (e), (g) and Cr-edge (d), (f), (h). The dips in the hysteresis loops at zero magnetic field are x-ray intensity artifacts which are typical for the TEY detection mode [54].

## VI. THEORETICAL RESULTS

The spin, orbital, and total magnetic moments of the Fe, Pt, and Cr atoms in the L1<sub>0</sub> (Fe<sub>100-x</sub>Cr<sub>x</sub>)Pt alloys, as obtained from the *ab initio* calculations ( $T = 0$  K) up to a concentration of 40 at. %, are summarized in Table III. As can be seen from this table, the magnetic moments of Fe, Cr, and Pt decrease slightly with increasing Cr content. Comparing these values with the experimental ones (see Table II), reasonable agreement is obtained considering that the experimental results

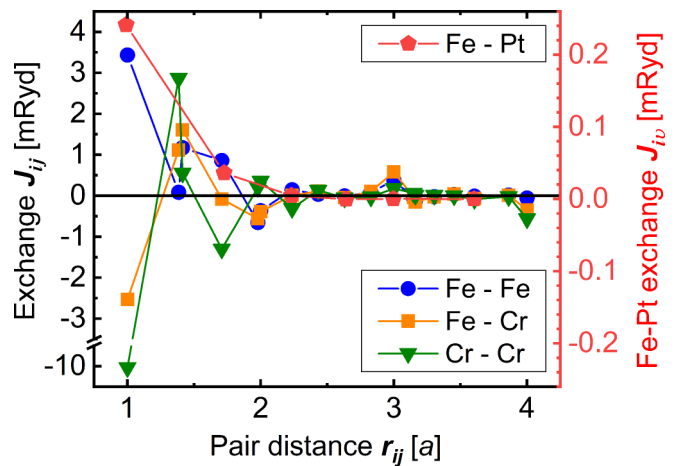


FIG. 9. *Ab initio* calculated exchange energies for Fe-Fe, Fe-Cr, Cr-Cr (left scale) and Fe-Pt (right scale) for (Fe<sub>90</sub>Cr<sub>10</sub>)Pt.

were obtained at room temperature and, also, represent spatial averages. Furthermore, it should be noted that the *ab initio* calculated spin moments of 3d elements using DFT-LSDA are in general overestimated compared to experimental values, as spin fluctuations are neglected [42]. The calculated uniaxial magnetic anisotropy constants displayed in Fig. 6(b) are systematically larger in magnitude than the experimental values. One reason for this deviation is that the calculations are performed for the ground state ( $T = 0$  K) while the static magnetic properties were measured at room temperature. It is well known both from experiment [55] and from theory [56,57] that the MAE of FePt decreases almost linearly with increasing temperature. The theoretical MAE monotonously decreases with increasing Cr concentration, however, the rapid breakdown of the experimental  $K_u$  above  $x = 20$  at. % is not recovered by the *ab initio* calculations. This can be attributed to the fact that the decrease of the order parameter  $S$  above 20 at. % [see Fig. 3(b)], was not included in the calculations, which is known to strongly reduce the MAE of FePt [55,56,58,59]. Next, the isotropic exchange interactions for the Fe-Fe, Cr-Cr, and Cr-Fe, as well as for the Fe-Pt pairs of atoms were calculated for the L1<sub>0</sub> (Fe<sub>100-x</sub>Cr<sub>x</sub>)Pt alloys, as exemplarily presented for  $x = 10$  at. % in Fig. 9. Most importantly, the NN Fe-Fe interaction is ferromagnetic, while the NN Fe-Cr and Cr-Cr interactions are antiferromagnetic, the latter being the largest one in magnitude. Furthermore, we found that the second-NN and also the fifth-NN Fe-Fe interactions that are interlayer couplings are antiferromagnetic, as also reported earlier [60]. These interactions would stabilize antiferromagnetic order of neighboring Fe layers. The ferromagnetic NN and NNN Fe-Pt couplings, see Fig. 9, however, stabilize ferromagnetic coupling between adjacent Fe layers. Since the induced moments of Pt are not considered in the spin-model [Eq. (5)], we employed the renormalization of the Fe-Fe interactions via the induced moments of Pt, as introduced by Mryasov *et al.* [57,61],

$$J_{ij} = J_{ij}^b + \frac{1}{S_{\text{FP}}} \sum_{\nu} J_{i\nu} J_{\nu j}, \quad (6)$$

TABLE III. *Ab initio* calculated spin moment ( $\mu_s$ ), orbital moment ( $\mu_l$ ), total magnetic moment ( $\mu_{\text{total}} = \mu_s + \mu_l$ ) of Fe, Cr, and Pt (per atom), saturation magnetization ( $M_S$ ), uniaxial magnetic anisotropy ( $K_u$ ), and the spin model simulated Curie temperatures ( $T_C$ ) of the  $(\text{Fe}_{100-x}\text{Cr}_x)\text{Pt}$  series.

Sample	Element	$\mu_s$ [ $\mu_B$ ]	$\mu_l$ [ $\mu_B$ ]	$\mu_{\text{total}}$ [ $\mu_B$ ]	$M_S$ [emu/cm <sup>3</sup> ]	$K_u$ [Merg/cm <sup>3</sup> ]	$T_C$ [K]
$(\text{Fe}_{95}\text{Cr}_5)\text{Pt}$	Fe	2.875	0.082	2.957	993	26.5	742
	Cr	2.530	0.018	2.548			
	Pt	0.287	0.046	0.332			
$(\text{Fe}_{89}\text{Cr}_{11})\text{Pt}$	Fe	2.868	0.083	2.951	873	25.2	719
	Cr	2.539	0.021	2.56			
	Pt	0.263	0.044	0.307			
$(\text{Fe}_{85}\text{Cr}_{15})\text{Pt}$	Fe	2.863	0.084	2.947	794	24.4	696
	Cr	2.543	0.023	2.566			
	Pt	0.248	0.043	0.291			
$(\text{Fe}_{80}\text{Cr}_{20})\text{Pt}$	Fe	2.853	0.085	2.938	693	23.2	672
	Cr	2.540	0.026	2.566			
	Pt	0.229	0.041	0.270			
$(\text{Fe}_{70}\text{Cr}_{30})\text{Pt}$	Fe	2.827	0.087	2.914	495	19.8	556
	Cr	2.504	0.030	2.534			
	Pt	0.188	0.037	0.225			
$(\text{Fe}_{60}\text{Cr}_{40})\text{Pt}$	Fe	2.799	0.089	2.888	317	14.9	417
	Cr	2.346	0.029	2.375			
	Pt	0.149	0.032	0.181			

where  $J_{ij}^b$  denotes the bare exchange interaction between the Fe atoms,  $J_{iv}$  stands for the exchange interaction between the Fe atom  $i$  and the Pt atom  $v$ , and  $S_{\text{FP}} = \sum_i J_{iv}$ . These renormalized Fe-Fe interactions are then displayed in Fig. 9. Though the fifth-NN Fe-Fe interaction is not affected by the renormalization, the first three Fe-Fe interactions are enhanced and, in particular, the second-NN Fe-Fe interaction became positive (ferromagnetic), as expected.

Based on the *ab initio* calculated  $J_{ij}$  and  $K_u$  values, the magnetic properties of the  $(\text{Fe}_{100-x}\text{Cr}_x)\text{Pt}$  system in the ground state was investigated. Our results suggest that at lower concentrations of Cr, the ground state forms a ferrimagnetic system due to the antiferromagnetic coupling between the Fe and Cr sublattices. However, as the concentration of Cr increases, the probability of finding nearest Cr-Cr pairs increases as well. Such spin arrangement makes the system a frustrated ferrimagnet due to the strong NN Cr-Cr antiferromagnetic coupling. In Fig. 10, the average angle of the ground-state normalized magnetic moments as a function of Cr concentration is plotted. Due to the exchange frustration in the system, the Cr spins are not exactly aligned antiparallel to Fe but show a canting behavior. While the canting angle of Fe changes only slightly with Cr content, a strong canting effect is observed for the Cr moment, resulting in a canting angle of up to about  $70^\circ$  with respect to the  $c$  axis at 40 at. %. Taking into account this canting effect, the saturation magnetization was determined which shows good agreement with the experimental results, as displayed in Fig. 6(c).

Starting from the ground-state spin configurations at zero temperature, the Curie temperatures of the  $(\text{Fe}_{100-x}\text{Cr}_x)\text{Pt}$  alloys were calculated. An example is presented in Fig. 11 also showing the variation of the magnetization with temperature for the two individual sublattices of Fe and Cr. For Cr concentration below 20%, the Curie temperature decreases rather slowly and stays within the temperature range of 650–750 K.

However, further increase of Cr concentration brings the Curie temperature to decrease rapidly, which is in excellent agreement with the experimental results [Fig. 7(b)].

## VII. CONCLUSIONS

Epitaxial pseudobinary  $(\text{Fe}_{100-x}\text{Cr}_x)\text{Pt}$  thin films were grown on MgO(001) covering the full composition range ( $x = 0 - 100$ ). As expected from the phase diagrams of the FePt and CrPt bulk alloys near equiatomic composition, Fe substitution by Cr in the  $L1_0$  structure with (001) orientation is obtained. However, beyond 20 at. % the chemical order parameter decreases continuously, as the deposition temperature of  $770^\circ\text{C}$  appears not to be sufficiently high for development of the  $L1_0$  CrPt phase. High perpendicular magnetic anisotropy and coercivity were observed with addition of up

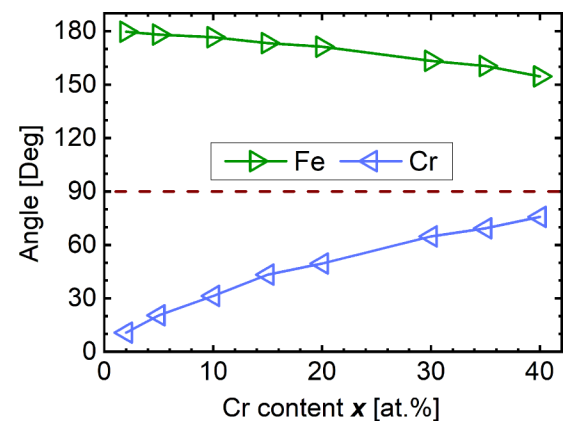


FIG. 10. The average angle of the ground-state spin moments with respect to the  $c$  axis shown as a function of Cr content for  $(\text{Fe}_{100-x}\text{Cr}_x)\text{Pt}$ .

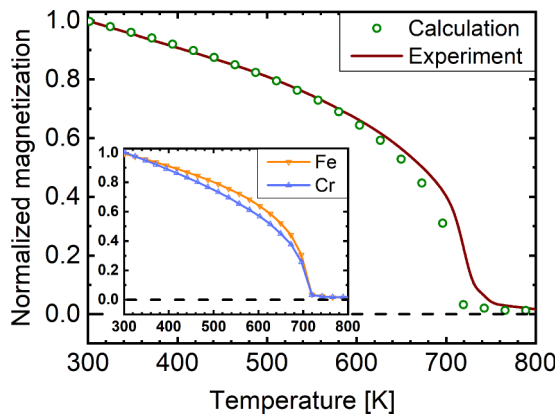


FIG. 11. Magnetization as a function of temperature for (Fe<sub>89</sub>Cr<sub>11</sub>)Pt. Green dots and red line denote theoretical and experimental values, respectively. The inset shows the temperature dependent magnetization of the two sublattices Fe and Cr.

to 20 at. % Cr. The change in coercivity is further attributed to a strong alteration of the film morphology changing from islandlike to a more continuous film structure.

Comparing our measurements with multiscale simulations, combining *ab initio* theory with spin-model simulations, we find that in dilute alloys with low Cr concentration, isolated Cr magnetic moments couple antiferromagnetically to the ferromagnetic Fe matrix, reducing the saturation magnetization. With increasing Cr concentration, nearest-neighbor Cr-Cr pairs start to appear, thereby increasing magnetic frustration and disorder. Frustration arises from the competition of ferromagnetic Fe-Fe, and antiferromagnetic Cr-Cr(Fe) nearest-neighbor exchange interactions, which lead to canting

of neighboring magnetic moments, as disclosed by our calculations. Furthermore, this effective exchange coupling will also impact the Curie temperature of the (Fe<sub>100-x</sub>Cr<sub>x</sub>)Pt alloy films. With Cr substitution of up to 20 at. %, no pronounced change in Curie temperature, which is in the range of 700 K, was noticed. But with addition of more than 35 at. % Cr, the Curie temperature drops down substantially. These results are in excellent agreement with our calculations.

Furthermore, XMCD studies on alloys containing up to 20 at. % of Cr confirmed strong antiferromagnetic exchange coupling between Fe and Cr and revealed spin magnetic moments in the range between 2.1– 2.5  $\mu_B$ , in reasonable agreement with *ab initio* calculations.

## ACKNOWLEDGMENTS

Financial support provided by the German Research Foundation (DFG) under Grants No. AL 618/31-1 and No. 290/5-1 are gratefully acknowledged. The authors are thankful for the allocation of synchrotron radiation beam time and acknowledge the financial support from HZB (Project No. 17105004-ST). We would like to thank O. Ciubutariu, M. Heigl, and R. Wendler for assistance at the HZB beamline and S. Rudorff for technical support, as well as F. Jung for assistance in SEM measurements. We are thankful for additional SEM measurement time at the CEITEC Nano Research Infrastructure with technical support from O. Man. L.S. is grateful for the financial support by the National Research Development and Innovation (NRDI) Office of Hungary under Project No. K131938 and also by the NRDI Fund TKP2020 IES (Grant No. BME-IE-NAT).

- [1] D. Weller, G. Parker, O. Mosendz, E. Champion, B. Stipe, X. Wang, T. Klemmer, G. Ju, and A. Ajan, *IEEE Trans. Magn.* **50**, 1 (2014).
- [2] D. Weller, G. Parker, O. Mosendz, A. Lyberatos, D. Mitin, N. Y. Safonova, and M. Albrecht, *J. Vac. Sci. Technol. B* **34**, 060801 (2016).
- [3] K. Hono, Y. K. Takahashi, G. Ju, J.-U. Thiele, A. Ajan, X. Yang, R. Ruiz, and L. Wan, *MRS Bull.* **43**, 93 (2018).
- [4] B. S. D. C. S. Varaprasad, Y. K. Takahashi, and K. Hono, *JOM* **65**, 853 (2013).
- [5] H. J. Richter and G. J. Parker, *J. Appl. Phys.* **121**, 213902 (2017).
- [6] R. Sbiaa, H. Meng, and S. N. Piramanayagam, *Phys. Status Solidi RRL* **5**, 413 (2011).
- [7] J. M. Slaughter, *Annu. Rev. Mater. Res.* **39**, 277 (2009).
- [8] Y. F. Ding, J. S. Chen, E. Liu, C. J. Sun, and G. M. Chow, *J. Appl. Phys.* **97**, 10H303 (2005).
- [9] J. Deng, H. Li, K. Dong, R.-W. Li, Y. Peng, G. Ju, J. Hu, G. M. Chow, and J. Chen, *Phys. Rev. Appl.* **9**, 034023 (2018).
- [10] H. Kim, J.-S. Noh, J. W. Roh, D. W. Chun, S. Kim, S. H. Jung, H. K. Kang, W. Y. Jeong, and W. Lee, *Nanoscale Res. Lett.* **6**, 13 (2010).
- [11] E. Yang, S. Ratanaphan, D. E. Laughlin, and J.-G. Zhu, *IEEE Trans. Magn.* **47**, 81 (2011).
- [12] T. Maeda, *IEEE Trans. Magn.* **41**, 3331 (2005).
- [13] C. Brombacher, H. Schletter, M. Daniel, P. Matthes, N. Jörmann, M. Maret, D. Makarov, M. Hietschold, and M. Albrecht, *J. Appl. Phys.* **112**, 073912 (2012).
- [14] M. Maret, C. Brombacher, P. Matthes, D. Makarov, N. Boudet, and M. Albrecht, *Phys. Rev. B* **86**, 024204 (2012).
- [15] D. A. Gilbert, L.-W. Wang, T. J. Klemmer, J.-U. Thiele, C.-H. Lai, and K. Liu, *Appl. Phys. Lett.* **102**, 132406 (2013).
- [16] Y. Takahashi, M. Ohnuma, and K. Hono, *J. Magn. Magn. Mater.* **246**, 259 (2002).
- [17] B.-H. Li, C. Feng, T. Yang, J. Teng, Z.-H. Zhai, G.-H. Yu, and F.-W. Zhu, *J. Phys. D: Appl. Phys.* **39**, 1018 (2006).
- [18] D. Mitin, M. Wachs, N. Safonova, O. Klein, and M. Albrecht, *Thin Solid Films* **651**, 158 (2018).
- [19] T. Ono, H. Nakata, T. Moriya, N. Kikuchi, S. Okamoto, O. Kitakami, and T. Shimatsu, *AIP Adv.* **6**, 056011 (2016).
- [20] R. Cuadrado, T. J. Klemmer, and R. W. Chantrell, *Appl. Phys. Lett.* **105**, 152406 (2014).
- [21] J. C. A. Huang, Y. C. Chang, C. C. Yu, Y. D. Yao, Y. M. Hu, and C. M. Fu, *J. Appl. Phys.* **93**, 8173 (2003).

- [22] K. Dong, X. Cheng, J. Yan, W. Cheng, P. Li, and X. Yang, *Rare Metals* **28**, 257 (2009).
- [23] M. L. Yan, Y. F. Xu, X. Z. Li, and D. J. Sellmyer, *J. Appl. Phys.* **97**, 10H309 (2005).
- [24] J.-U. Thiele, K. R. Coffey, M. F. Toney, J. A. Hedstrom, and A. J. Kellock, *J. Appl. Phys.* **91**, 6595 (2002).
- [25] G. Meyer and J.-U. Thiele, *Phys. Rev. B* **73**, 214438 (2006).
- [26] J. Park, Y.-K. Hong, S.-G. Kim, L. Gao, and J.-U. Thiele, *J. Appl. Phys.* **117**, 053911 (2015).
- [27] D. B. Xu, J. S. Chen, T. J. Zhou, and G. M. Chow, *J. Appl. Phys.* **109**, 07B747 (2011).
- [28] I. Mirebeau, V. Pierron-Bohnes, C. Decorse, E. Rivière, C.-C. Fu, K. Li, G. Parette, and N. Martin, *Phys. Rev. B* **100**, 224406 (2019).
- [29] T. Suzuki, H. Kanazawa, and A. Sakuma, *IEEE Trans. Magn.* **38**, 2794 (2002).
- [30] J. B. J. Chapman, P.-W. Ma, and S. L. Dudarev, *Phys. Rev. B* **99**, 184413 (2019).
- [31] S. J. Pickart and R. Nathans, *J. Appl. Phys.* **34**, 1203 (1963).
- [32] P. C. Kuo, Y. D. Yao, C. M. Kuo, and H. C. Wu, *J. Appl. Phys.* **87**, 6146 (2000).
- [33] E. Yang, D. E. Laughlin, and J. Zhu, *IEEE Trans. Magn.* **48**, 7 (2012).
- [34] J.-U. Thiele, L. Folks, M. F. Toney, and D. K. Weller, *J. Appl. Phys.* **84**, 5686 (1998).
- [35] T. Noll and F. Radu, in *9th Mechanical Engineering Design of Synchrotron Radiation Equipment and Instrumentation* (JACoW Publishing, Geneva, Switzerland, 2017), pp. 370–373.
- [36] S. H. Vosko, L. Wilk, and M. Nusair, *Can. J. Phys.* **58**, 1200 (1980).
- [37] L. Szunyogh, B. Újfalussy, P. Weinberger, and J. Kollár, *Phys. Rev. B* **49**, 2721 (1994).
- [38] R. Zeller, P. H. Dederichs, B. Újfalussy, L. Szunyogh, and P. Weinberger, *Phys. Rev. B* **52**, 8807 (1995).
- [39] L. Szunyogh, B. Újfalussy, and P. Weinberger, *Phys. Rev. B* **51**, 9552 (1995).
- [40] L. Udvardi, L. Szunyogh, K. Palotás, and P. Weinberger, *Phys. Rev. B* **68**, 104436 (2003).
- [41] P. Ravindran, A. Kjekshus, H. Fjellvaag, P. James, L. Nordström, B. Johansson, and O. Eriksson, *Phys. Rev. B* **63**, 144409 (2001).
- [42] A. B. Shick and O. N. Mryasov, *Phys. Rev. B* **67**, 172407 (2003).
- [43] P. Soven, *Phys. Rev.* **156**, 809 (1967).
- [44] A. Lyberatos, D. V. Berkov, and R. W. Chantrell, *J. Phys.: Condens. Matter* **5**, 8911 (1993).
- [45] U. Nowak, *Handbook of Magnetism and Advanced Magnetic Materials* (Wiley, Chichester, 2007).
- [46] K. Watanabe, *Permanent Magnet Properties and their Temperature Dependence in the Fe-Pt-Nb Alloy System* (Materials Transactions, The Japan Institute of Metals and Materials, 1991) Vol. 32, pp. 292–298.
- [47] H. W. King, *J. Mater. Sci.* **1**, 79 (1966).
- [48] V. Petkov, Y. Maswadeh, J. A. Vargas, S. Shan, H. Kareem, Z.-P. Wu, J. Luo, C.-J. Zhong, S. Shastri, and P. Kenesei, *Nanoscale* **11**, 5512 (2019).
- [49] R. Zhang, R. Skomski, X. Li, Z. Li, P. Manchanda, A. Kashyap, R. D. Kirby, S.-H. Liou, and D. J. Sellmyer, *J. Appl. Phys.* **111**, 07D720 (2012).
- [50] M. Futamoto, M. Nakamura, M. Ohtake, N. Inaba, and T. Shimotsu, *AIP Adv.* **6**, 085302 (2016).
- [51] A. Dannenberg, M. E. Gruner, A. Hucht, and P. Entel, *Phys. Rev. B* **80**, 245438 (2009).
- [52] R. A. Evarestov and A. V. Bandura, *Int. J. Quantum Chem.* **100**, 452 (2004).
- [53] D. J. Srolovitz and M. G. Goldiner, *JOM* **47**, 31 (1995).
- [54] E. Goering, A. Fuss, W. Weber, J. Will, and G. Schütz, *J. Appl. Phys.* **88**, 5920 (2000).
- [55] S. Okamoto, N. Kikuchi, O. Kitakami, T. Miyazaki, Y. Shimada, and K. Fukamichi, *Phys. Rev. B* **66**, 024413 (2002).
- [56] J. B. Staunton, S. Ostanin, S. S. A. Razee, B. Gyroffly, L. Szunyogh, B. Ginatempo, and E. Bruno, *J. Phys.: Condens. Matter* **16**, S5623 (2004).
- [57] O. N. Mryasov, U. Nowak, K. Y. Guslienko, and R. W. Chantrell, *Europhys. Lett.* **69**, 805 (2005).
- [58] C. Aas, L. Szunyogh, J. Chen, and R. Chantrell, *Appl. Phys. Lett.* **99**, 132501 (2011).
- [59] A. Deák, E. Simon, L. Balogh, L. Szunyogh, M. dos Santos Dias, and J. B. Staunton, *Phys. Rev. B* **89**, 224401 (2014).
- [60] C. J. Aas, P. J. Hasnip, R. Cuadrado, E. M. Plotnikova, L. Szunyogh, L. Udvardi, and R. W. Chantrell, *Phys. Rev. B* **88**, 174409 (2013).
- [61] O. N. Mryasov, *Phase Transit.* **78**, 197 (2005).